



Research Paper

Cocatalyst free Z-schematic enhanced H₂ evolution over LaVO₄/BiVO₄ composite photocatalyst using Ag as an electron mediator



Naveen Kumar Veldurthi^{a,*}, Neerugatti KrishnaRao Eswar^b, Satyapaul A. Singh^a, Giridhar Madras^a

^a Department of Chemical Engineering, Indian Institute of Science, Bangalore, India

^b Centre for Nanoscience and Engineering, Indian Institute of Science, Bangalore, India

ARTICLE INFO

Keywords:
Z-scheme
Redox mediator free
LaVO₄/BiVO₄
Cocatalyst free
H₂ evolution

ABSTRACT

A novel cocatalyst free Z-schematic photocatalytic system of Ag/LaVO₄/BiVO₄ was successfully fabricated for clean hydrogen fuel evolution. The spherical nanoparticles of LaVO₄ were prepared in solution combustion method for the first time using glycine as a fuel. BiVO₄ was deposited onto LaVO₄ through a deposition–precipitation method and Ag was loaded on the surface of LaVO₄/BiVO₄ composite by photoreduction method. The composites were characterized by XRD, UV–vis DRS, SEM, TEM, EDS and XPS to ensure the successful integration of Ag or (and) BiVO₄ with LaVO₄. A series of photocatalytic H₂ evolution experiments, employing Na₂S and Na₂SO₃ as hole scavengers, showed that the Ag/LaVO₄/BiVO₄ composite exhibited a superior photocatalytic performance compared to single LaVO₄ or BiVO₄. Although BiVO₄ cannot be used for H₂ evolution, it can significantly enhance the H₂ evolution performance of LaVO₄ through a Z-scheme mechanism with Ag as an electron mediator. Moreover, investigations on photoluminescence and fluorescence lifetime measurements demonstrated the greater separation efficacy of photoinduced excitons in the Z-scheme Ag/LaVO₄/BiVO₄ photocatalytic system. This newly constructed LaVO₄ based Z-scheme system exhibits promising photocatalytic H₂ evolution activity with significant longevity and will be useful for potential applications in energy driven technologies.

1. Introduction

Hydrogen has been heralded as a clean and sustainable fuel with zero carbon emission and high energy yield (141.9 MJ/kg) than conventional fuels [1]. Solar light driven photocatalytic water splitting to produce hydrogen has become a promising solution to the tapering resources of fossil fuels and detrimental effects of greenhouse gases produced due to their combustion. Strenuous attempts have been carried out to enhance the visible light absorption of the conventional photocatalysts such as TiO₂, ZnO etc. which are just active under UV-light irradiation [2–4]. However, it is obvious that mere visible light absorption will not guarantee higher photocatalytic efficacy. Typically, the performance of photocatalysts is significantly favored by three conditions: (i) a narrow band gap that can facilitate the efficient utilization of sunlight (ii) a more negative conduction band (CB) potential and a more positive valence band (VB) potential for the reduction and oxidation reactions, respectively (iii) reducing the rate of recombination of photogenerated charge carriers [5]. However, condition (ii) will widen the band gap of a photocatalyst, resulting poor sunlight

absorption i.e., incongruity of condition (i). Therefore, it is difficult for a single semiconductor photocatalyst to simultaneously possess broad solar light-absorption, enhanced separation of charge carriers and strong redox ability.

In addition, most semiconductors cannot produce H₂ without a cocatalyst (often Pt), even by using sacrificial electron donor [6]. The indispensable need of expensive noble metal cocatalyst, to localize the protons for the formation of hydrogen gas, is another factor that makes the photocatalytic water splitting a rather unfeasible proposition [7]. In this context, there is an urgent quest for designing cocatalyst free composite photocatalytic systems, without compromising with the efficiency, by prudently choosing the relative band positions of the two photocatalysts for efficient utilization of solar energy and limiting the rate of recombination of photogenerated charge carriers.

Besides tuning the photocatalyst itself, the coupling of two semiconductors in staggered alignment of band structures provides more separation of photogenerated excitons. As a result of irradiation, the two conjoint semiconductors in a heterojunction composite photocatalyst are activated simultaneously. The photogenerated electrons are

* Corresponding author.

E-mail addresses: naveen.veldurthi@gmail.com, vnaveen@IISc.ac.in (N.K. Veldurthi).

transferred from a higher conduction band to a lower conduction band, whereas the holes transport to a higher valence band from a lower valence band. Thus designing heterojunction photocatalysts has emerged as the inevitable route to achieve efficient charge separation [8]. However, increment in the separation of charge carriers occurs while dampening the redox ability, due to the photogenerated electrons and holes are accumulated on the band with lower redox potentials [9]. It is difficult to achieve strong redox ability and higher electron-hole separation simultaneously by the heterojunction composite photocatalysts.

Z-scheme water splitting mimicking photosynthesis of green plants was first introduced by Bard in 1979 [10]. Since then many efforts have been made to construct Z-scheme photocatalytic systems without redox mediators (i.e., liquid ionic pairs such as IO_3^-/I^- , $\text{Fe}^{3+}/\text{Fe}^{2+}$ and $\text{Co}(\text{bpy})_3^{3+}/\text{Co}^{2+}$) causing backward reactions [11,12]. In 2006, an all solid state Z-scheme system of $\text{CdS}-\text{Au}-\text{TiO}_2$ was reported for the first time, using Au as an electron mediator between two photocatalysts [13]. As no redox couples were used, the stability and the charge transfer was simultaneously improved. In direct Z-scheme system of two narrow band gap photocatalysts, photogenerated electrons of one semiconductor with a lower conduction band and holes of other semiconductor with a higher valence band are recombined. Therefore, Z-scheme photocatalyst (with or without electron mediator) not only boosts the separation efficiency of photogenerated electron-hole pairs, but also preserves excellent redox ability.

More recently, significant attention has been paid to the monoclinic lanthanum vanadate (m-LaVO₄) owing to its notable properties such as light absorption in the visible region and surface catalytic ability [14,15]. However, its utilization in the photocatalytic hydrogen generation has not been reported so far. LaVO₄-based photocatalysts suffer from certain limitations such as lower surface area and the quick recombination of photogenerated excitons. Based on the above considerations, BiVO₄ has been chosen to couple with LaVO₄ to remedy the defect of faster recombination of charge carriers thereby improving the photocatalytic efficiency. BiVO₄ has several merits such as visible light absorption, chemical stability, low cost and non-toxic properties [16]. BiVO₄ alone is unable to produce hydrogen through water splitting because its conduction band is located at a more positive potential than the potential of water reduction [0 eV Vs NHE; H^+/H_2]. However, considering the composite of LaVO₄/BiVO₄, it is expected to enhance the rate of H₂ evolution through the Z-scheme mechanism. Furthermore, previous reports suggest that LaVO₄ has suitable band edges ($E_{\text{CB}} = -0.06$ eV, $E_{\text{VB}} = 2.01$ eV), that match well with BiVO₄ band edge positions ($E_{\text{CB}} = 0.46$ eV, $E_{\text{VB}} = 2.86$ eV) to probably form a direct Z-scheme photocatalytic system [17,18].

The poor interfacial charge transfer efficiency has a negative influence on the electron–hole separation ability. In particular, BiVO₄ is known for poor electron conductivity [19]. Therefore, an effective conductive charge mediator is essential at the interface of LaVO₄-BiVO₄ for attaining high efficiency. For instance, Ag has been used as such electron mediator in many Z-scheme systems because of its excellent electron conductivity [20–22]. Ag has been chosen as an electron mediator as it is cheaper than other electron mediators such as Au, Ru, Pd, Ir and Pt. Further, the Fermi level of metallic Ag is more negative than the valence band of LaVO₄, more positive than conduction band of BiVO₄. Thus, Ag makes a good charge transfer bridge between LaVO₄ and BiVO₄. Therefore, in the current work, LaVO₄ and BiVO₄ was combined with and without Ag to construct a novel solid-state Z-scheme photocatalytic system for H₂ evolution from water using Na₂S and Na₂SO₃ solution as a sacrificial agent. Moreover, the present Z-scheme photocatalytic system avoids the inherent requirement of the expensive noble metal cocatalyst to generate hydrogen. The essence of the thermodynamic relationship between LaVO₄ and BiVO₄ is explained and the mechanism of effective charge separation based on the Z-scheme fashion is also studied in detail.

2. Experimental

2.1. Synthesis

Monoclinic LaVO₄ was prepared by solution combustion method for the first time using glycine as a fuel. Solution combustion is a one step self-propagating synthesis method. In this method, reactant mixture is ignited to a temperature that is considerably lower than the actual phase formation temperature in a short time and it is considered as one of the energy efficient preparative methods [23–25]. The precursor solution was made by dissolving stoichiometric amounts of $\text{La}(\text{NO}_3)_3 \cdot 6\text{H}_2\text{O}$ (1.705 g) and NH_4VO_3 (0.46 g) in 15 mL of water and 5 mL of 3 M nitric acid, respectively. Both were mixed in a combustion petri dish and stirred with magnetic stirrer. Stoichiometric amount of glycine (0.55 g) was dissolved in 10 mL of water and added to the above mixture. This solution mixture was placed into a muffle furnace held at 400 °C for 20 min. The obtained product was heated in furnace at 500 °C for 2 h to obtain pure lanthanum vanadate powders. The product yield is approximately 1 g.

The LaVO₄/BiVO₄ composite photocatalysts were prepared by a facile deposition-precipitation method [26]. Typically, 0.2 g of LaVO₄ was dispersed in 30 mL of deionized water using ultrasonication. Subsequently, $\text{Bi}(\text{NO}_3)_3$ and NH_4VO_3 were precisely weighed with the molar ratio of 1:1 and were individually dissolved in a 3 M nitric acid solution. Then, the two solutions were mixed well and the pH was adjusted to 9 by slowly adding NaOH solution. An orange yellow precipitate was obtained and then it was blended with the LaVO₄ suspension under vigorous stirring for 12 h. The final product was obtained by filtering the precipitate followed by sintering at 500 °C for 5 h. The composites with different weight ratios of LaVO₄ to BiVO₄ were LaVO₄/BiVO₄ (10 wt%), LaVO₄/BiVO₄ (20 wt%), LaVO₄/BiVO₄ (30 wt%) and LaVO₄/BiVO₄ (50 wt%), which are labeled as LV/BV10, LV/BV20, LV/BV30 and LV/BV50, respectively. The bare monoclinic BiVO₄ sample was also synthesized under the same conditions without adding LaVO₄.

In addition, Ag deposited LaVO₄/BiVO₄ composite was prepared by photodeposition method. The previously prepared LV/BV20 was added into 50 mL of 10 vol% methanol solution. After that, calculated amount of AgNO_3 was added, and the suspension was irradiated with a 400 W metal halide lamp for 60 min. The product was washed with ethanol and water for three times, and dried at 60 °C. Ag/LaVO₄ was also prepared by the same procedure by depositing 10 wt% of Ag on LaVO₄.

2.2. Characterizations

X-ray diffraction patterns were recorded on a Bruker D8 diffractometer using $\text{Cu}-\text{K}\alpha$ radiation at a scan rate of 2°/min in the 20°–80° scan range. Diffuse reflectance spectral studies were performed using solid state UV-vis spectrophotometer (PerkinElmer, Lambda 35). ULTRA55 FESEM, Carl Zeiss was used to obtain SEM images. Prior to taking images, the samples drop-casted on silicon wafers, they were dispersed in absolute ethanol and ultrasonicated for 5 min. The drop-casted samples were gold sputtered using Quorum sputtering before imaging in order to restrict charging of the sample. TEM images were captured using FEI Tecnai T-20 operated at 180 kV. TEM samples were dispersed in absolute ethanol and drop-casted onto copper grids. X-ray photoelectron spectra were obtained using ESCA+, (omicron nanotechnology, Oxford Instrument Germany). Powder samples were deposited on Cu tape and degassed for overnight in XPS FEL chamber to avoid the air contamination on sample surface. A charge neutralizer of 2 keV is applied to overcome the charging problem and binding energy of C1 s core at 284.6 eV was considered as reference. Photoluminescence spectra were obtained using a PerkinElmer LS 55 Luminescence spectrophotometer. Time-resolved fluorescence emission decay measurements of the samples were collected on a FLS980 Fluorescence Spectrometer (Edinburgh Instruments) and the excitation

wavelength was set to 340 nm. BET surface area measurements were performed using Nova-1000 Quantachrome after the catalysts were regenerated at 120 °C for 2 h. Electrochemical experiments were carried out using a CH Instruments potentiostat/galvanostat (model 608C) in 0.1 M Na₂SO₄ electrolyte at a frequency of 1 kHz in dark in a conventional three-electrode configuration with the catalyst drop casted on indium tin oxide (ITO)-coated glass as working electrode, a platinum wire as the counter electrode and a saturation calomel electrode (SCE) as the reference electrode.

2.3. Evaluation of photocatalytic H₂ generation

The photocatalytic H₂ evolution experiments were performed in a photoreactor, consisting a 400 W metal halide lamp that was placed inside a cylindrical quartz jacket and cooled using water circulation. The metal halide lamp was chosen intentionally because it adequately replicates both the pattern and intensity of peaks of the solar spectrum thus simulating the solar illumination with a very low UV-A content and a large part in the visible region [27,28]. In a typical experiment, 0.015 g of the catalyst powders was dispersed in a quartz vessel containing 150 mL of freshly prepared 0.5 M Na₂S + 0.5 M Na₂SO₃ solution. Prior to irradiation, the suspension was thoroughly degassed to remove air by bubbling Ar gas for 30 min. The hydrogen content was analyzed by gas chromatograph (Mayura Analytical, India) with high-purity Ar as a carrier gas using TCD detector.

3. Results and discussion

3.1. Characterization studies

Lanthanum vanadate was prepared by a solution-combustion process using glycine as a fuel. Glycine is a complexing agent and inhibits the agglomeration of the metal ions as the water is evaporated. Glycine is oxidized by the nitrate ions (oxidizers) and it caters as a fuel for the combustion process. In this synthesis, dissolution of La(NO₃)₃ in the aqueous medium results in La³⁺ ions and NH₄VO₃ in nitric acid produces VO₃⁻ ions. Glycine becomes a zwitter ion with both positive amino group end and the negative carboxylic end in aqueous solution. After adding glycine solution, the mixture of La³⁺ and VO₃⁻ ions form the metal chelate complex by attaching to the bidentate ligand of the glycine molecules [29]. When the metal chelate complex is subjected to high temperature, auto combustion process initiates and it breaks down the complex to form fine crystallites with the evolution of N₂, H₂O and CO₂ gases. These gases quickly evolve to break large clusters, hindering particle growth and thereby increasing porosity of synthesized nanomaterials. The resulting powders after auto-ignition were calcined at 500 °C for 2 h to obtain pure and well crystalline LaVO₄.

The phase purity of the as prepared LaVO₄ and co-occurrence of both LaVO₄ and BiVO₄ phases in the composite photocatalysts were investigated using the powder XRD technique. It is observed that all the diffraction peaks of LaVO₄ (Fig. 1(a)) can be readily indexed to a perfect monoclinic structure (JCPDS No. 70-0216) and no other peaks corresponding to the ingredients are observed. It can also be seen that the LaVO₄/BiVO₄ composites exhibit similar XRD patterns to pure LaVO₄. No diffraction peaks of BiVO₄ are discerned for LaVO₄/BiVO₄ (10 wt%) in Fig. 1(b), probably due to the small amount of BiVO₄. When the weight of BiVO₄ is larger than 10% in the composite, the XRD patterns show a diffraction peak at 2θ = 28.6°, which is attributed to the monoclinic BiVO₄ phase (JCPDS No. 14-0688). The intensity of this peak increases with the amount of the BiVO₄ loading, indicating that more BiVO₄ particles are deposited on the surface of LaVO₄. The diffraction peaks of BiVO₄ are denoted with asterisk symbols. The diffraction peaks of two distinct phases of LaVO₄ and BiVO₄ are clearly observed in the XRD pattern of LV/BV50 as shown in Fig. 1(e). The XRD patterns of monoclinic BiVO₄ prepared by precipitation method are also presented for comparison in Fig. 1(g). Moreover, the diffraction peak

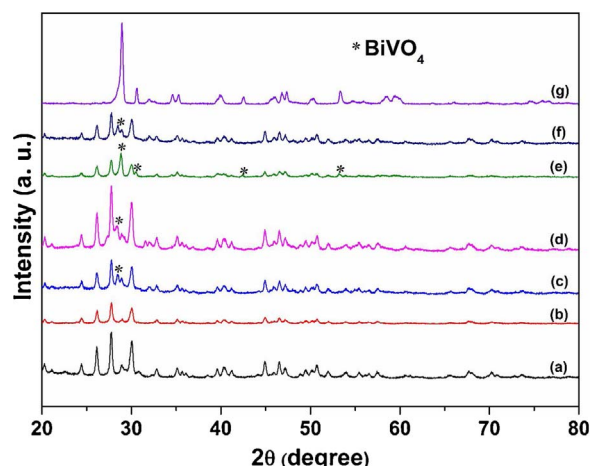


Fig. 1. Powder X-ray diffraction patterns of (a) LaVO₄, (b) LV/BV10, (c) LV/BV20, (d) LV/BV30, (e) LV/BV50, (f) Ag/LV/BV20 and (g) BiVO₄.

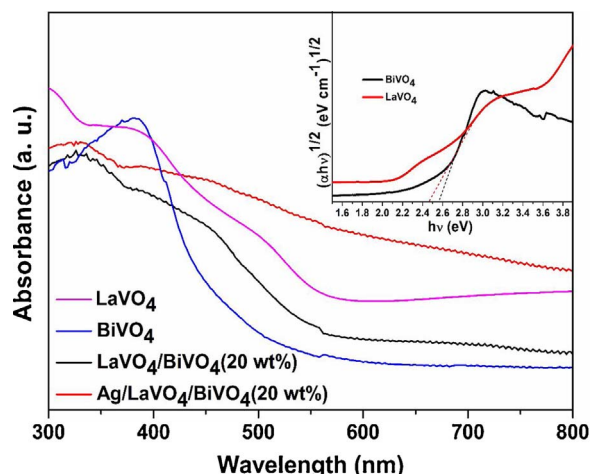


Fig. 2. UV-vis diffuse reflectance spectra of photocatalysts and inset shows Kubelka-Munk-transformed DRS of LaVO₄ and BiVO₄.

positions of LaVO₄ do not shift, which suggests BiVO₄ is merely deposited on the surface of LaVO₄ instead of covalently merging into the crystal lattice. In addition, the XRD pattern of Ag/LaVO₄/BiVO₄ (20 wt%) (Fig. 1(f)) is similar to that of LaVO₄/BiVO₄ (20 wt%) (Fig. 2(c)), and no distinguishable peaks corresponding to metallic Ag are observed, because the amount of Ag loading in the composite is possibly below the detection limit of XRD. The presence of metallic Ag on the surface of LaVO₄/BiVO₄ (20 wt%) composite has been verified in the later section. Therefore, up to now, the above analyses endorse the coexistence of both LaVO₄ and BiVO₄ in the composite photocatalysts.

The photoresponse of a semiconductor, which is inextricably linked to its electronic structure, is considered as the key factor in determining its photocatalytic activity. The optical property of LaVO₄, BiVO₄, LaVO₄/BiVO₄ (20 wt%) and Ag/LaVO₄/BiVO₄ (20 wt%) was investigated using UV-vis diffuse reflectance spectra ranging from ultraviolet to visible region, as shown in Fig. 2. It is clearly seen in Fig. 2 that all the samples show strong absorbance in the visible region. Particularly, the absorption curve of the Ag/LaVO₄/BiVO₄ (20 wt%) shows distinctly enhanced visible-light absorption compared to other catalysts. The monoclinic phases of both LaVO₄ and BiVO₄ can be regarded as indirect band gap semiconductors [30,31] and their band gap energies can be determined using the plot of the Kubelka-Munk function $(\alpha h\nu)^{1/2}$ versus incident light energy $(h\nu)$, where α is absorption co-efficient, h is Planck constant and ν is frequency of light [32]. The extrapolated linear line of the curve that meets at x-axis intercept gives

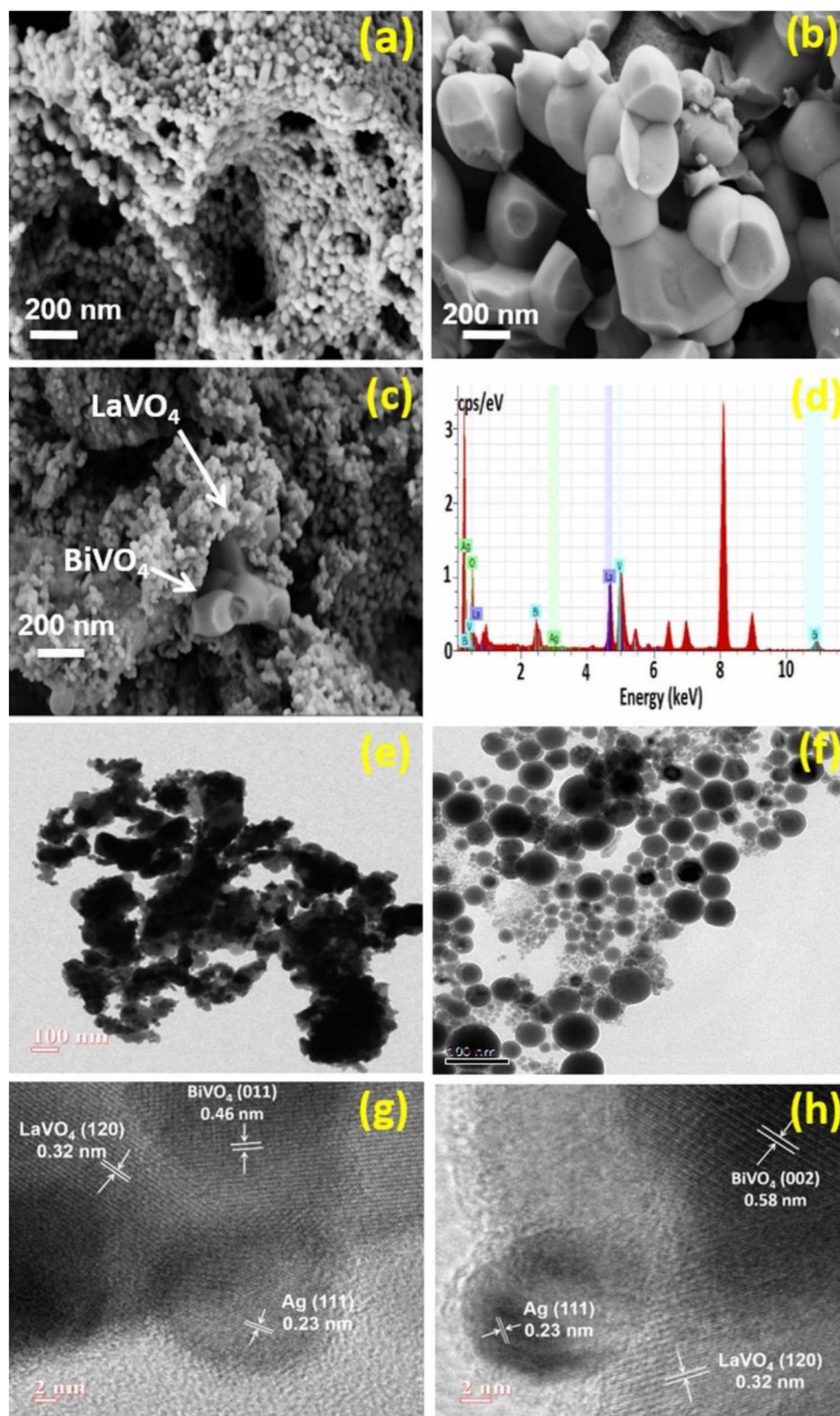


Fig. 3. SEM images of (a) LaVO_4 , (b) BiVO_4 , (c) LV/BV20, (d) EDS profile of Ag/LV/BV20, bright field TEM images of (e) Ag/LV/BV20 and (f) LaVO_4 , HR-TEM images (g, h) of Ag/LV/BV20.

band gap energy of LaVO_4 and BiVO_4 as shown in the inset of Fig. 2. By applying this equation, the band gap of LaVO_4 and BiVO_4 is estimated to be 2.48 eV and 2.56 eV, respectively.

The band gap of the LaVO_4 synthesized in this work is found to be slightly higher (~ 0.4 eV) compared to that of the bulk LaVO_4 , [15,18,33] which can be ascribed to the quantum confinement effect in

the nanocrystalline LaVO_4 . In general, higher band gap energy for at least one counterpart of the composite could be beneficial for improving the redox potential of photocatalytic reaction, importantly for water splitting. In the present investigation, both LaVO_4 and BiVO_4 have narrow band gaps with no significant difference, suggesting that band alignment of the catalysts is the decisive factor in designing Z-

scheme photocatalysts rather than disparity in the band gap energies.

To determine the morphology and microstructure of the composite and its counterparts, scanning electron microscopy (SEM) and transmission electron microscopy (TEM) images were recorded at room temperature as shown in Fig. 3. LaVO₄ exhibits network of nanoparticle assemblages, as shown in Fig. 3(a) and the TEM image (Fig. 3(f)) also confirms that spherical nanoparticles of LaVO₄ are dense and non uniform ranging in size from 5 to 80 nm. The morphology of pure BiVO₄ displays irregular shaped crystallites, as shown in Fig. 3(b). These crystallites possess well exposed smooth surfaces and sharp edges which play considerable role in charge carrier migration. In the SEM image of LV/BV20 (Fig. 3(c)), both LaVO₄ and BiVO₄ particles are easily distinguishable and LaVO₄ particles are well anchored with the surface of BiVO₄. Therefore, the formation of LaVO₄/BiVO₄ composite is obviously discernible that is beneficial to the efficient transport of charge carriers in comparison to pure LaVO₄.

The TEM image of Ag/LV/BV20 in Fig. 3(e) displays the aggregation of large BiVO₄ particles with smaller LaVO₄ particles and metallic Ag particles with size of about 10 nm are deposited on the surface of composite. Moreover, metallic Ag particles are formed on the junction of LaVO₄ and BiVO₄ evidenced by the three sets of lattice fringes as shown in the HRTEM images (Fig. 3(g, h)) of Ag/LV/BV20 composite photocatalyst. The d-spacings of BiVO₄, LaVO₄ and Ag in Ag/LV/BV20 were determined as 0.46/0.58 nm, 0.32 nm and 0.23 nm from the lattice fringes of (011)/(002), (120) and (111) planes corresponding to monoclinic BiVO₄, LaVO₄ and cubic Ag, respectively. Noticeably, the connections among these components are intimate and Ag particles mostly exist at the interface of LaVO₄ and BiVO₄. The latter is probably due to the photogenerated electron diffusion at the interface of LaVO₄/BiVO₄ during the photodeposition of Ag [34]. Therefore, Ag can act as an electron mediator between LaVO₄ and BiVO₄ in the composite photocatalyst. In addition, TEM equipped energy dispersive spectrum (EDS) in Fig. 3(d) verifies that Ag, La, Bi, V and O are the only elements detected in the Ag/LV/BV20 photocatalyst. The measured BET surface areas of LaVO₄, BiVO₄, LV/BV20 and Ag/LV/BV20 are found to be 3.2, 2.3, 4.7 and 4.6 m²/g, respectively. The BET surface areas exhibited little difference between pure LaVO₄ and Ag/LV/BV20, which indicates that the photocatalytic performance of catalysts cannot be judged by the differences in their surface areas in the present investigation. Therefore, the BET experiments ruled out the contribution of surface area in improving the photocatalytic activity of the composite.

The X-ray photoelectron spectroscopy (XPS) survey spectrum of Ag/LV/BV20 (Fig. 4(a)) exhibits the presence of Ag, La, Bi, V, O and C elements, indicating its hybrid composition. Among them, the presence of the C element may be due to the hydrocarbon contaminants that commonly exist for XPS. The chemical states of all elements of Ag/LV/BV20 sample were analyzed by their high-resolution XPS spectra, as shown in Fig. 4(b–f). Two signals at 834.9 eV and 851.7 eV in Fig. 4(c) are ascribed to La 3d_{5/2} and La 3d_{3/2}, respectively, which can be assigned to La³⁺ ion of LaVO₄ [35]. The binding energies of Bi 4f_{7/2} and Bi 4f_{5/2} are 159.08 eV and 164.2 eV, respectively (Fig. 4(d)), confirming that bismuth is in the +3 valence state in BiVO₄ lattice [36]. The observed O 1s peaks at 530.1 eV and 531.9 eV in Fig. 4(f) are in agreement with the lattice oxygen and oxygen species of hydroxyl groups adsorbed on the surface, respectively [37]. The binding energies of V 2p_{3/2} and V 2p_{1/2} are observed at 517.0 eV and 524.2 eV (Fig. 4(e)), respectively, which can be attributed to V⁵⁺ ions of VO₄³⁻ moieties in the LaVO₄ and BiVO₄ samples [14,36]. These results confirmed the coexistence of LaVO₄ and BiVO₄ in Ag/LV/BV20 sample, which is consistent with the XRD analysis. Moreover, Ag 3d spectrum clearly indicates two characteristic peaks at 368.1 eV and 374.1 eV as shown in Fig. 4(b), corroborating the presence of metallic Ag on the surface of the LV/BV20 sample [38]. Therefore, it can be inferred that the Ag particles have been formed on the surface of the LV/BV20 photocatalyst during the photoreduction process and which can act as electron mediator in the composite photocatalyst.

To further elucidate the interactions between LaVO₄ and BiVO₄ in Ag/LV/BV20, the high-resolution XPS spectra of La 3d of pristine LaVO₄, Bi 4f of pure BiVO₄ and Ag/LV/BV20 are shown in Fig. 4(g, h). The binding energies of Bi 4f_{7/2} and Bi 4f_{5/2} of BiVO₄ are shifted by 0.4 eV with respect to Ag/LV/BV20. Similarly, the binding energies of the La 3d_{5/2} and La 3d_{3/2} of pure LaVO₄ are shifted by 0.45 eV compared to Ag/LV/BV20. This shift in binding energies is a consequence of the formation of an interface between LaVO₄ and BiVO₄, which causes disturbance in the electron density and the local environment around the elements. Based on these XPS results, it is believed that LaVO₄ and BiVO₄ interact electronically through the interface and metallic Ag particles have been successfully loaded on the surface of LV/BV20 composite, to fabricate a Z-scheme Ag/LV/BV20 photocatalytic system.

3.2. Photocatalytic hydrogen evolution

The evaluation of photocatalytic performances for H₂ evolution of LaVO₄, Ag/LaVO₄, BiVO₄ and LaVO₄/BiVO₄ composites are shown in Fig. 5. Pristine BiVO₄ did not produce any hydrogen due to the more positive conduction band potential. However, when BiVO₄ is coupled with LaVO₄, enhanced photocatalytic efficiency of LaVO₄ was observed for H₂ evolution. All the composite photocatalysts and pristine LaVO₄ exhibit significant photocatalytic activities of H₂ evolution without any cocatalyst, unveiling the inherent photocatalytic H₂ generation property of LaVO₄ for the first time. After 3 h of irradiation, the corresponding H₂ evolution for LaVO₄ is 24 μmol h⁻¹, which is relatively low because of the easy annihilation of photoexcited electron-hole pairs. In addition, Ag (10 wt%) deposited LaVO₄ (Ag/LaVO₄) shows slightly higher photocatalytic activity than pure LaVO₄. However, Ag/LaVO₄ shows lower photocatalytic H₂ evolution than the LaVO₄/BiVO₄ composites, which imply that combining LaVO₄ and BiVO₄ is an efficient route to improve the photocatalytic activity of LaVO₄ than mere loading of Ag on LaVO₄. With the increased loading of BiVO₄ to 20 wt% (LV/BV20), the H₂ evolution rate is enhanced to 45.5 μmol h⁻¹, revealing the synergism between BiVO₄ and LaVO₄.

However, the H₂ evolution for LaVO₄/BiVO₄ decreased gradually with the further increase in the amount of BiVO₄ loading. The reason for reduction of activity may be envisaged as the excess of BiVO₄ on the surface of LaVO₄ may mask the active sites for hydrogen generation. Through the sequential increase in loading of BiVO₄ components, it has been found that the 20 wt% of BiVO₄ onto LaVO₄ (LV/BV20) as optimal loading since it exhibited the higher photocatalytic activity. In addition, the H₂ evolution rate of LV/BV20 is noticeably enhanced by Ag loading. When the loading of Ag is 10 wt% with respect to LV/BV20, the H₂ evolution rate reached a maximum of 55.8 μmol h⁻¹ and that sample is denoted as Ag/LV/BV20. This may signify that Ag could play as a crucial charge carrier bridge between LaVO₄ and BiVO₄ that results in enhancement of charge separation efficiency for LaVO₄. The activity trend (Fig. 6) indicates that after a threshold Ag loading (10 wt%), the H₂ evolution rate declines, which may be credited to the overloading of Ag particles. The Ag in the over loaded samples renders the parasitic absorption which block the transition of photons in the LV/BV20 thereby generation of photogenerated charge carriers, finally could account for decreased activity [6]. In addition, a control experiment with Ag (10 wt%) deposited physically ground mixture of LaVO₄/BiVO₄(20 wt%) showed a very low yield of hydrogen than Ag/LV/BV20 (as shown in Fig. 6(e)). It clearly demonstrates that the firm contact formed between the counterparts of the composite played key role in enhancing the hydrogen evolution rate of Ag/LV/BV20.

Moreover, the BET surface areas exhibited diminutive difference among LaVO₄, BiVO₄, LV/BV20 and Ag/LV/BV20, which indicates that the specific surface areas had little effect on the photocatalytic performance of the samples. Therefore, all the above observations evince that the charge carrier dynamics occurring at the interface between the LaVO₄ and BiVO₄ may be decisive for the photocatalytic H₂ production. At this stage, it was thought worthwhile to ensure the broader utility of

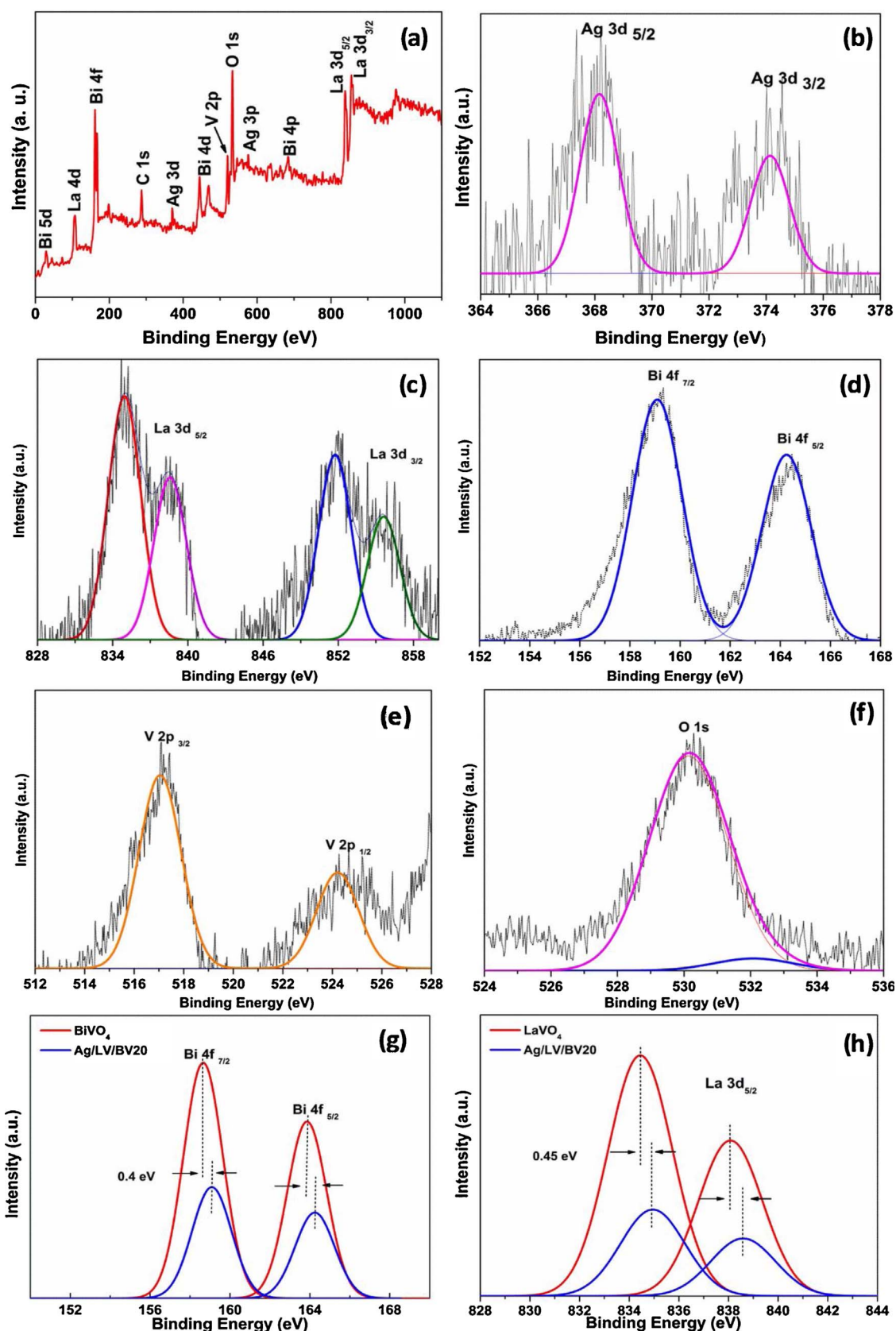


Fig. 4. XPS spectra of sample Ag/LV/BV20: (a) the survey spectrum, (b) Ag 3d, (c) La 3d, (d) Bi 4f, (e) V 2p, (f) O 1s, (g) comparison of Bi 4f of pure BiVO₄ and Ag/LV/BV20 (h) comparison of La 3d of pure LaVO₄ and Ag/LV/BV20.

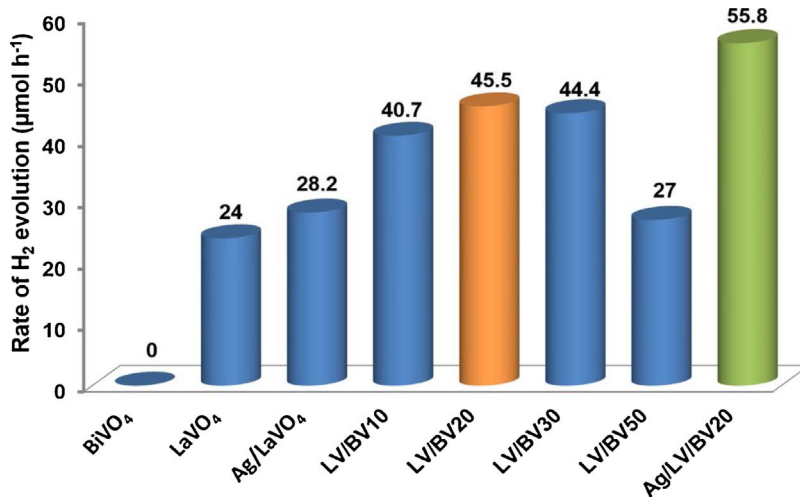


Fig. 5. Rate of H_2 evolution for various photocatalysts during 3 h of irradiation.

the current materials and their activities were compared with the results of redox mediator free Z-scheme photocatalyst systems reported in literature as shown in Table 1. Most of the reported Z-scheme photocatalysts used very expensive Pt as cocatalyst or Au as electron mediator or both, which may hinder their use for practical applications.

Based on the above outcomes, LaVO₄/BiVO₄ composite photocatalysts possessed implicitly a higher photocatalytic hydrogen evolution rate than its individual counterparts. For the sake of clarifying the detailed root causes of the improved performance of the composite photocatalyst, knowledge of relative band edge positions of the catalysts is crucial. The migration pathway of the photogenerated charge carriers across the interface of LaVO₄/BiVO₄ composite depends on the band edge position of the two semiconductors. The valence band (VB) and the conduction band (CB) of the both catalysts in LaVO₄/BiVO₄ composite were calculated empirically using Mulliken absolute electronegativity (χ) and the band gap of a semiconductor obtained using DRS [60,61]. The χ value for LaVO₄ is 5.69 and the E_{CB} and E_{VB} of LaVO₄ are calculated to be -0.05 and 2.43 eV, respectively. The CB position of LaVO₄ is found to be negative than the hydrogen electrode potential (0 eV Vs NHE; H^+ / H_2) to achieve the prerequisite of the hydrogen evolution and it is in agreement with the previous report [18]. The same principle can be applied to calculate the band edge positions of BiVO₄ and the obtained E_{CB} and E_{VB} are 0.23 and 2.79 eV, respectively, which clearly supports the thermodynamic inability of BiVO₄ to produce hydrogen.

In addition, Mott–Schottky method was also used to determine the CB and VB of both LaVO₄ and BiVO₄, which has been considered as reliable technique for determination of electronic potentials of semiconductors [62,63]. The flatband potential of a semiconductor can be obtained from the x-intercept of the linear region of the Mott–Schottky

plots as shown in Fig. 7. The flatband potentials of LaVO₄ and BiVO₄ were approximately calculated as -0.28 and -0.06 V (vs. SCE), respectively. The obtained flatband potentials can be converted to the normal hydrogen electrode (NHE) scale via the Nernst equation (Eq. (1)):

$$E(\text{NHE}) = E(\text{SCE}) + 0.24 \quad (1)$$

The calculated E_{CB} of LaVO₄ and BiVO₄ were -0.04 eV and 0.18 eV, respectively. The E_{VB} of LaVO₄ and BiVO₄ were calculated using their band gap energies as shown in Eq. (2) and E_{VB} of LaVO₄ and BiVO₄ were 2.44 and 2.74 eV, respectively.

$$E_g = E_{VB} - E_{CB} \quad (2)$$

The band edge potentials of LaVO₄ and BiVO₄ obtained from Mott–Schottky plots are consistent with the values calculated from Mulliken absolute electronegativity (χ) and the band gap. Therefore, these results strongly conclude that CB bottom of LaVO₄ was higher than that of BiVO₄, whereas VB top of BiVO₄ was lower than that of LaVO₄.

Based on the band alignments of LaVO₄ and BiVO₄, Scheme 1 plots the two kinds of possible electron – hole transfer mechanisms in LaVO₄/BiVO₄ composite: (i) customary heterojunction-type and (ii) direct Z-scheme type. In both cases, two semiconductors are activated simultaneously by irradiation. If the charge carrier migration in LaVO₄ and BiVO₄ occurs through a conventional heterojunction mechanism, the photoinduced electrons in CB of LaVO₄ can transport to the CB of BiVO₄, whereas the photoinduced holes in the VB of BiVO₄ move to the VB of LaVO₄ as shown in Scheme 1(a). Because of the positive E_{CB} of BiVO₄, the photoinduced electrons accumulated in the CB of BiVO₄ cannot produce hydrogen. However, the results of present

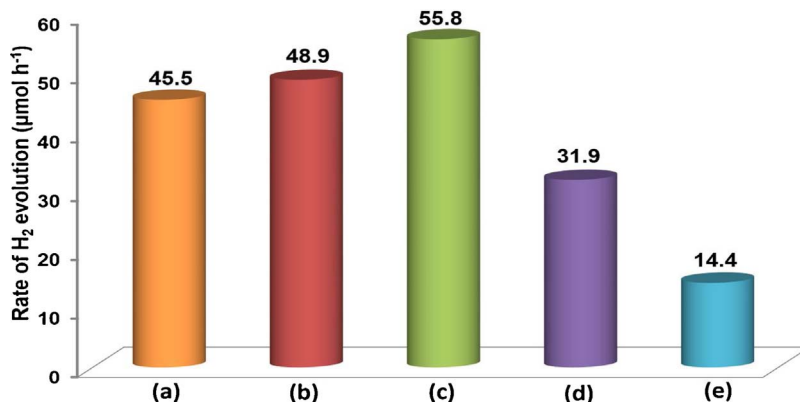
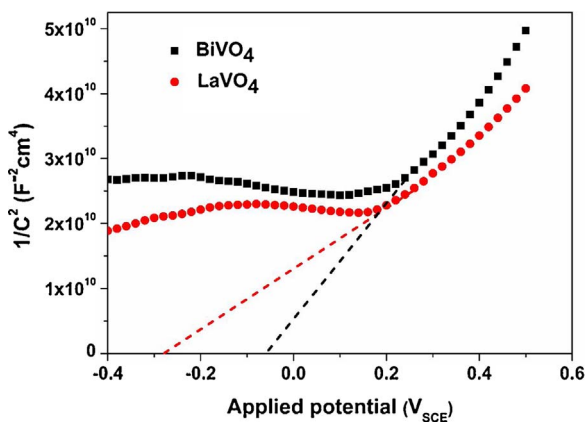


Fig. 6. Rate of H_2 evolution for different loadings of Ag on LV/BV20; (a) LV/BV20, (b) Ag(5 wt%)/LV/BV20, (c) Ag(10 wt%)/LV/BV20, (d) Ag(15 wt%)/LV/BV20, (e) Ag(10 wt%) on physical mixture of LV/BV20.

Table 1

Redox mediator free Z-scheme photocatalysts for hydrogen evolution reported in the literature. (PS – Photosystem, Cocat – Cocatalyst).

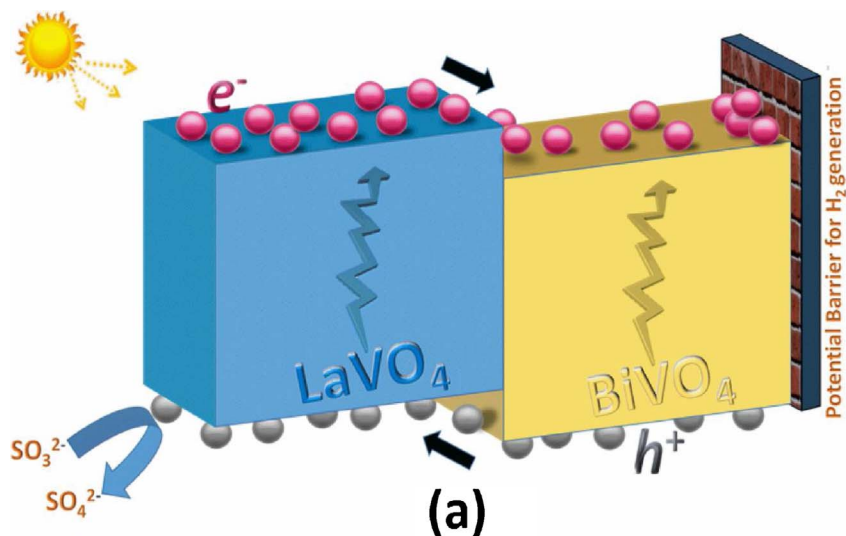
S. No	PS-I	PS-II	Cocat.	Electron mediator	Light source	Catalyst loading/Reactant solution	Application	Activity ($\mu\text{mol h}^{-1}$)	Refs.
1.	TiO ₂	CdS	Pt	Au	500 W Xe lamp ($300 < \lambda < 400$)	0.02 g/20 mL water	H ₂ production	0.01	[13]
2.	TiO _{1.96} C _{0.04}	CdS	Pt	Au	Xe arc lamp (> 420)	0.15 g/150 mL Na ₂ S (0.05 M) + Na ₂ SO ₃ (0.1 M)	H ₂ production	433.2	[39]
3.	WO ₃	PbBi ₂ Nb _{1.9} Ti _{0.1} O ₉	–	W	450 W Xe arc lamp (> 420)	0.3 g/170 mL water + 30 mL CH ₃ OH	H ₂ production	14.7	[40]
4.	BiVO ₄	SrTiO ₃ :Rh	Ru	RGO	300 W Xe lamp (> 420)	0.03 g/120 mL H ₂ SO ₄ (pH 3.5)	water splitting	H ₂ : 11 O ₂ : 5.5	[41]
5.	TiO ₂	CdS	–	Au	750 W Xe-illuminator (full)	0.05 g/50 mL Na ₂ S (0.25 M) + Na ₂ SO ₃ (0.35 M)	H ₂ production	3.2	[42]
6.	ZnO	CdS	–	Au	300 W Xe lamp (full)	0.1 g/270 mL Na ₂ S (0.1 M) + Na ₂ SO ₃ (0.1 M)	H ₂ production	60.8	[43]
7.	TiO ₂	P ₂ W ₁₇	–	Pt	250 W high pressure Hg lamp (> 365)	0.05 g/8 mL glycerol + 72 mL water	H ₂ production	19.6	[44]
8.	ZnO	CdS	Pt	Cd	300 W Xe lamp (full)	0.1 g/300 mL Na ₂ S (0.1 M) + Na ₂ SO ₃ (0.1 M)	H ₂ production	1920	[45]
9.	BiVO ₄	SrTiO ₃ :Rh	Ru	–	300 W Xe arc lamp (> 420)	0.1 g/120 mL water (H ₂ SO ₄ , pH 3.5)	water splitting	H ₂ : 29 O ₂ : 14	[46]
10.	Ir/CoO _x /Ta ₃ N ₅	SrTiO ₃ :Rh	Ru	Ir	300 W Xe lamp (> 420)	0.05 g/250 mL water (H ₂ SO ₄ , pH 4.9)	water splitting	H ₂ : 23 O ₂ : 12	[47]
11.	ZnO	CdS	Pt	–	300 W Xe lamp (full)	0.2 g/300 mL Na ₂ S (0.1 M) + Na ₂ SO ₃ (0.1 M)	H ₂ production	774	[48]
12.	g-C ₃ N ₄	WO ₃	Pt	–	300 W Xe lamp (> 420)	0.04 g/40 mL 10 vol% triethanolamine	H ₂ production	4.4	[49]
13.	ZnRh ₂ O ₄	Ag _{1-x} SbO _{3-y}	–	Ag	300 W Xe lamp (> 460)	0.06 g/12 mL water	water splitting	H ₂ : 0.38 O ₂ : 0.2	[50]
14.	CuGaS ₂	TiO ₂	Pt	RGO	300 W Xe lamp (full)	0.05 g/120 mL water	water splitting	H ₂ : 19.8 O ₂ : 10.3	[51]
15.	TiO ₂	MoO ₃	Pt	–	75 W Xe lamp (full)	0.1 g/300 mL methanol	H ₂ production	16	[52]
16.	ZnIn ₂ S ₄	g-C ₃ N ₄	–	Nano C	12 W UV-LED($= 420$)	0.05 g/80 mL 0.5 M Na ₂ S + 0.5 M Na ₂ SO ₃	H ₂ production	50.3	[53]
17.	CoTiO ₃	g-C ₃ N ₄	Pt	–	300 W Xe lamp (full)	0.02 g/10 vol% ethanol	H ₂ production	17.1	[54]
18.	Cu ₂ O	g-C ₃ N ₄	–	Pd	300 W Xe lamp ($400 < \lambda < 780$)	0.015 g/20 mL 10 vol% triethanolamine	H ₂ production	0.48	[55]
19.	CdS	WO ₃	Pt	–	500 W Xe lamp(> 400)	0.05 g/lactic acid	H ₂ production	145	[56]
20.	LaMg _{1/3} Ta _{2/3} O ₂ N	BiVO ₄ :Mo	RhCrO _x	Au	300 W Xe lamp(> 400)	0.02 g/40 mL 20% methanol, 40 mL 20 mM AgNO ₃	water splitting	H ₂ : 1.2 O ₂ : 0.6	[57]
21.	RGO	Ag ₃ PO ₄	–	–	300 W Xe lamp(> 400)	0.05 g/50 mL 10% methanol	H ₂ production	184	[58]
22.	Si	MgTiO ₃	–	–	300 W Xe lamp(> 420)	0.02 g/100 mL of pure water	H ₂ production	3.18	[59]
23.	LaVO ₄	BiVO ₄	–	–	400 W Metal halide lamp	0.015 g/150 mL 0.5 M Na ₂ S + 0.5 M Na ₂ SO ₃	H ₂ production	45.5	Present work
24.	LaVO ₄	BiVO ₄	–	Ag	400 W Metal halide lamp	0.015 g/150 mL 0.5 M Na ₂ S + 0.5 M Na ₂ SO ₃	H ₂ production	55.8	Present work

**Fig. 7.** Mott-Schottky plots collected for LaVO₄ and BiVO₄ at a frequency of 1 kHz in the dark. (0.1 M Na₂SO₄, vs SCE).

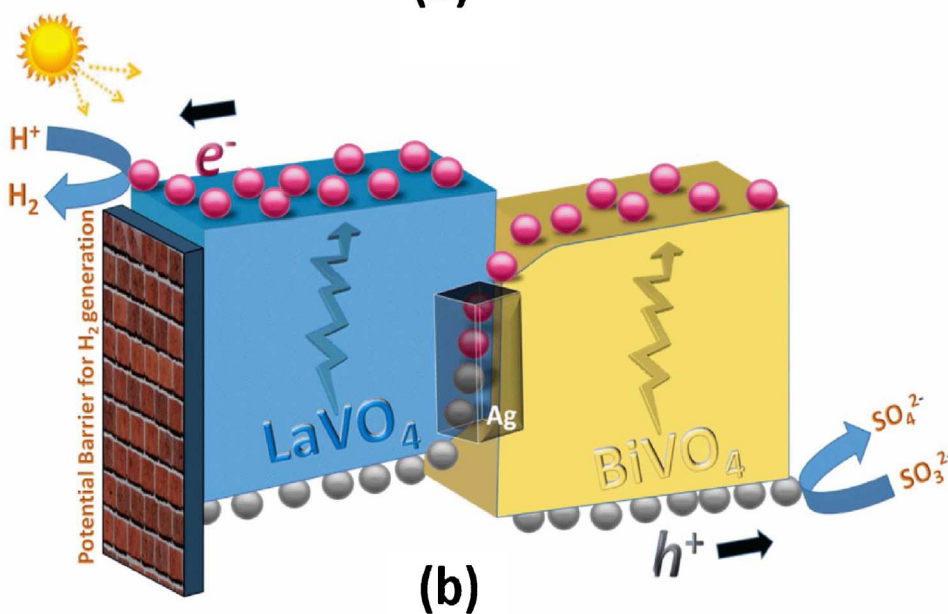
photocatalytic H₂ production experiments conflict the conventional heterojunction mechanism. Therefore, photocatalytic hydrogen can be generated in the LaVO₄/BiVO₄ composite only when the electrons in the CB of BiVO₄ are ready or forced to migrate to the VB of LaVO₄ by the Z-scheme mechanism. In this process, weak reductive electrons in

CB of BiVO₄ are recombined with the weak oxidative holes in VB of LaVO₄. Thus, the photogenerated electrons with strong reducibility are accumulated on the conduction band of LaVO₄, which have the energy to stride over the potential barrier and reduce H⁺ into H₂ gas. Meanwhile the photogenerated holes with strong oxidizability are accumulated on the valence band of BiVO₄ and they are funneled to be consumed by the sacrificial reagent. Therefore, it can be impeccably confirmed that the proposed mechanism of direct Z-scheme is reasonable for LaVO₄/BiVO₄ composite.

In addition, the interfacial charge transfer efficiency of LV/BV20 composite was further improved by loading Ag as a charge transmission bridge. During the internal charge transmission, the electrons in the CB of BiVO₄ move to metallic Ag due to the E_{CB} of BiVO₄ is quite negative than the Fermi level of metallic Ag (i.e., 0.8 eV) [64]. Concurrently, the holes in the VB of LaVO₄ shift to metallic Ag owing to the E_{VB} of LaVO₄ is far positive than the Fermi level of metallic Ag and mingle with electrons here as shown in **Scheme 1(b)**. Therefore, the intimate contact between LaVO₄ and BiVO₄ with the nested band edge positions and Ag as the charge transmission bridge act in concert to promote more reductive electrons for H₂ evolution, which is presumed to be the origin of the observed superior photocatalytic activity of Ag/LV/BV20. It is reported in the literature that Z-scheme charge transfer mechanism can be verified by the overall water splitting in presence of composite photocatalyst and in the absence of electron acceptor and donor [65].



(a)



(b)

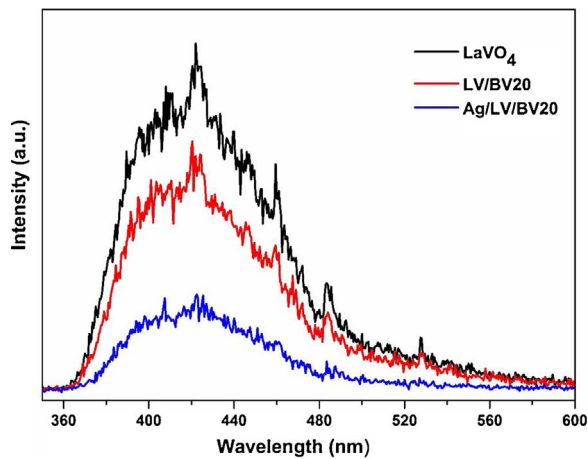


Fig. 8. Room-temperature photoluminescence (PL) emission spectra of LaVO_4 , LV/BV20 and Ag/LV/BV20 composites excited at 340 nm.

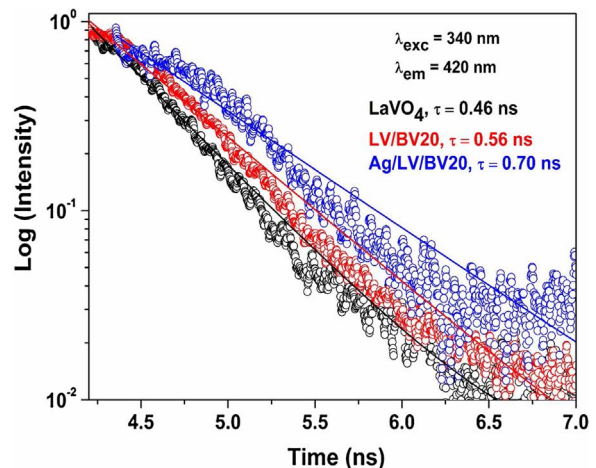


Fig. 9. PL decay measurements of photocatalysts. τ is the lifetime obtained by fitting to a single exponential decay function.

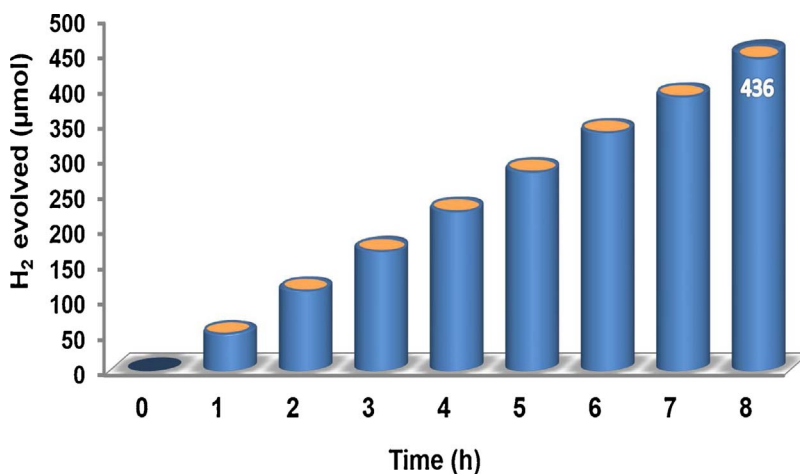


Fig. 10. Hydrogen generation over Ag/LV/BV20 with the irradiation time of 8 h.

The evaluation of overall water splitting using Ag/LV/BV20 photocatalyst was carried out with pure water under similar experimental conditions without adding any sacrificial reagent. The rates of hydrogen and oxygen evolution are observed to be $1.17 \mu\text{mol h}^{-1}$ and $0.52 \mu\text{mol h}^{-1}$, respectively. Therefore, the simultaneous evolution of hydrogen and oxygen in aqueous reactant solution with Ag/LV/BV20 photocatalyst is consistent with the Z-scheme charge transfer mechanism. The very low yield of hydrogen and oxygen gases is obvious in overall water splitting because it is an uphill reaction associated with the rapid recombination of photogenerated electrons – holes and large driving force for the backward reaction producing H_2O [66]. To meet the objective of this work (i.e., generation of hydrogen fuel), photocatalytic hydrogen evolution was studied with Na_2S and Na_2SO_3 as hole scavengers and the rate of hydrogen evolution is almost 50 times more than the rate of hydrogen evolution in overall water splitting.

To validate the efficient separation of charge carriers in Z-scheme $\text{LaVO}_4/\text{BiVO}_4$ composite, photoluminescence (PL) spectra have been studied. PL spectroscopy is directly related to the dynamic behavior of photogenerated charge carriers, such as transfer, capture and separation, because PL signal is a result of recombination of free charge carriers [67,68]. There is a consensus regarding the correlation between PL emission intensity and photocatalytic performance, that the life time of photogenerated charge carriers is longer for weaker PL signal. Thus, charge carriers have a greater possibility to reach the surface of catalyst to initiate the redox reactions. Upon exciting at 340 nm, a broad emission peak of LaVO_4 was detected around 420 nm, which indicates that the electrons and holes recombine rapidly in LaVO_4 . The intensity of the luminous peak of LV/BV20 is weaker than that of LaVO_4 as shown in Fig. 8, which conquers the recombination of the photogenerated electrons and holes to some extent. The intensity of the PL peak of Ag/LV/BV20 shows a further decay by comparing with that of the LV/BV20 composite. This indicates that the existence of Ag in this composite can effectively increase the lifetime of the photogenerated electrons that can participate in the reduction reaction instead of emissive recombination. This is in good agreement with the superior photocatalytic hydrogen evolution of Ag/LV/BV20.

To shed more light on the lifetime of the photogenerated electron–hole pair in the photocatalysts, the decay profiles of the emission were obtained using time-resolved fluorescence spectroscopy. In the fluorescence decay profiles (Fig. 9), LaVO_4 showed relatively short life time of excited electrons which means the characteristic higher rate of recombination of electron–hole pairs. LV/BV20 exhibited a longer life time of excited electrons than LaVO_4 suggesting that transfer of photoexcited electrons and holes between LaVO_4 and BiVO_4 must exist in a Z-scheme manner and that retards the annihilation of charge carriers. The lifetime of carriers in Ag/LV/BV20 is further prolonged which promotes Ag as an electron mediator on $\text{LaVO}_4/\text{BiVO}_4$ composite and it

could also be concluded that photocatalytic results are in line with the lifetime measurements.

The Z-scheme Ag/LV/BV20 photocatalyst also showed stable H_2 evolution behavior over a period of 8 h, as shown in Fig. 10. Moreover, the nearly linear increase in cumulative hydrogen evolution with the irradiation time was noticed and reached up to 436 μmol in 8 h, which entails the sustainable photocatalytic hydrogen generation. The structural integrity of the photocatalyst is retained even after 8 h of photocatalytic run as evident from XRD patterns (not shown), implying the excellent phase stability. Hence, the Z-scheme Ag/LV/BV20 photocatalyst exhibits excellent H_2 evolution activity with significant longevity.

4. Conclusions

The present work investigated the ability of LaVO_4 to evolve hydrogen for the first time in aqueous Na_2S and Na_2SO_3 solution and the construction of LaVO_4 based Z-scheme $\text{Ag}/\text{LaVO}_4/\text{BiVO}_4$ photocatalytic system without the use of cocatalysts and redox mediators. Ag loaded $\text{LaVO}_4/\text{BiVO}_4$ (20 wt%) showed a higher rate of hydrogen evolution compared to Ag/LaVO_4 and $\text{LaVO}_4/\text{BiVO}_4$ (20 wt%), indicating the crucial role of Ag as electron mediator. The superior photocatalytic performance of $\text{Ag}/\text{LaVO}_4/\text{BiVO}_4$ is mainly ascribed to the enhanced life span of charge carriers in a Z-scheme charge-transfer mechanism originating from the well-nested band positions of LaVO_4 and BiVO_4 despite their closer band gap energies. The Z-scheme charge-transfer mechanism and role of Ag as an electron mediator were further testified by photoluminescence and life time measurements. In summary, this contribution provides an avenue for designing novel and highly efficient Z-scheme photocatalysts, thus meeting the requirements of future energy driven technologies.

Acknowledgements

GM thanks Department of Science and Technology (DST) for J. C. Bose fellowship. NKV is grateful to DST-Science and Engineering Research Board (SERB) for the award of National Post Doctoral Fellowship (PDF/2016/000155). The authors thank Dr. Anshu Pandey, Solid State and Structural Chemistry Unit, IISc for extending Time-resolved fluorescence facility. The authors thank Ms. Rimzhim Gupta and Ms. Noopur Jain for their assistance in PL, DRS and BET measurements, respectively. The authors thank Prof. N. Munichandraiah and Mr. Brij Kishore, Department of Inorganic and Physical Chemistry, IISc for Electrochemical measurements.

References

- [1] Hydrogen Analysis Resource Center, (2017) Accessed 06 March 2017 <http://hydrogen.pnl.gov/tools/lower-and-higher-heating-values-fuels>.
- [2] S.m. Chang, W.s. Liu, Surface doping is more beneficial than bulk doping to the photocatalytic activity of vanadium-doped TiO_2 , *Appl. Catal. B: Environ.* 101 (2011) 333–342.
- [3] Q. Kang, S. Liu, L. Yang, Q. Cai, C.A. Grimes, Fabrication of PbS nanoparticle-sensitized TiO_2 nanotube arrays and their photoelectrochemical properties, *ACS Appl. Mater. Interfaces* 3 (2011) 746–749.
- [4] G. Yang, Z. Jiang, H. Shi, T. Xiao, Z. Yan, Preparation of highly visible-light active N-doped TiO_2 photocatalyst, *J. Mater. Chem.* 20 (2010) 5301–5309.
- [5] J. Li, N. Wu, Semiconductor-based photocatalysts and photoelectrochemical cells for solar fuel generation: a review, *Catal. Sci. Technol.* 5 (2015) 1360–1384.
- [6] H. Cheng, X.-J. Lv, S. Cao, Z.-Y. Zhao, Y. Chen, W.-F. Fu, Robustly photogenerating H_2 in water using FeP/CdS catalyst under solar irradiation, *Sci. Rep.* 6 (2016) 19846.
- [7] BASF. <https://apps.catalysts.bASF.com/apps/eibprices/mp/>, 2017 (Accessed 06 March 2017).
- [8] R. Marschall, Semiconductor composites: strategies for enhancing charge carrier separation to improve photocatalytic activity, *Adv. Funct. Mater.* 24 (2014) 2421–2440.
- [9] C. Ren, J. Fan, S. Liu, W. Li, F. Wang, H. Li, X. Liu, Z. Chang, One-step hydrothermal synthesis of novel $\text{Ag}_3\text{VO}_4/\text{Ag}_8\text{V}_2\text{O}_7$ composites for enhancing visible-light photocatalytic performance, *RSC Adv.* 6 (2016) 95156–95164.
- [10] A.J. Bard, Photoelectrochemistry and heterogeneous photo-catalysis at semiconductors, *J. Photochem.* 10 (1979) 59–75.
- [11] M. Higashi, R. Abe, T. Takata, K. Domen, Photocatalytic overall water splitting under visible light using ATaO_2N ($\text{A} = \text{Ca, Sr Ba}$) and WO_3 in a IO_3^-/I^- shuttle redox mediated system, *Chem. Mater.* 21 (2009) 1543–1549.
- [12] K. Sayama, K. Mukasa, R. Abe, Y. Abe, H. Arakawa, A new photocatalytic water splitting system under visible light irradiation mimicking a Z-scheme mechanism in photosynthesis, *J. Photochem. Photobiol. A* 148 (2002) 71–77.
- [13] H. Tada, T. Mitsui, T. Kiyonaga, T. Akita, K. Tanaka, All-solid-state Z-scheme in $\text{CdS}-\text{Au}-\text{TiO}_2$ three-component nanojunction system, *Nat. Mater.* 5 (2006) 782–786.
- [14] X. Liu, H. Qin, W. Fan, Enhanced visible-light photocatalytic activity of a $\text{g-C}_3\text{N}_4/\text{m-LaVO}_4$ heterojunction: band offset determination, *Chin. Sci. Bull.* 61 (2016) 645–655.
- [15] X. Zou, X. Li, Q. Zhao, S. Liu, Synthesis of $\text{LaVO}_4/\text{TiO}_2$ heterojunction nanotubes by sol-gel coupled with hydrothermal method for photocatalytic air purification, *J. Colloid Interface Sci.* 383 (2012) 13–18.
- [16] Y. Kim, D. Shin, W.J. Chang, H.L. Jang, C.W. Lee, H.E. Lee, K.T. Nam, Hybrid Z-scheme using photoystem I and BiVO_4 for hydrogen production, *Adv. Funct. Mater.* 25 (2015) 2369–2377.
- [17] X. Gao, H.B. Wu, L. Zheng, Y. Zhong, Y. Hu, X.W.D. Lou, Formation of mesoporous heterostructured $\text{BiVO}_4/\text{Bi}_2\text{S}_3$ hollow discoids with enhanced photoactivity, *Angew. Chem. Int. Ed.* 53 (2014) 5917–5921.
- [18] Y. He, J. Cai, L. Zhang, X. Wang, H. Lin, B. Teng, L. Zhao, W. Weng, H. Wan, M. Fan, Comparing two new composite photocatalysts $\text{t-LaVO}_4/\text{g-C}_3\text{N}_4$ and $\text{m-LaVO}_4/\text{g-C}_3\text{N}_4$, for their structures and performances, *Ind. Eng. Chem. Res.* 53 (2014) 5905–5915.
- [19] J.H. Kim, J.S. Lee, BiVO_4 -based heterostructured photocatalysts for solar water splitting: a review, *Energy Environ. Focus* 3 (2014) 339–353.
- [20] F. Chen, Q. Yang, X. Li, G. Zeng, D. Wang, C. Niu, J. Zhao, H. An, T. Xie, Y. Deng, Hierarchical assembly of graphene-bridged $\text{Ag}_3\text{PO}_4/\text{Ag}/\text{BiVO}_4$ (040) Z-scheme photocatalyst: an efficient sustainable and heterogeneous catalyst with enhanced visible-light photoactivity towards tetracycline degradation under visible light irradiation, *Appl. Catal. B: Environ.* 200 (2017) 330–342.
- [21] X. Lin, J. Hou, S. Jiang, Z. Lin, M. Wang, G. Che, A Z-scheme visible-light-driven $\text{Ag}/\text{Ag}_3\text{PO}_4/\text{Bi}_2\text{MoO}_6$ photocatalyst: synthesis and enhanced photocatalytic activity, *RSC Adv.* 5 (2015) 104815–104821.
- [22] Y. Wang, C.-G. Niu, L. Zhang, Y. Wang, H. Zhang, D.-W. Huang, X.-G. Zhang, L. Wang, G.-M. Zeng, High-efficiency visible-light $\text{AgI}/\text{Ag}/\text{Bi}_2\text{MoO}_6$ as a Z-scheme photocatalyst for environmental applications, *RSC Adv.* 6 (2016) 10221–10228.
- [23] A.K. Alves, C.P. Bergmann, F.A. Berutti, Novel Synthesis and Characterization of Nanostructured Materials, Springer-Verlag, Berlin, Heidelberg, 2013.
- [24] K. Nagaveni, M. Hegde, N. Ravishankar, G. Subbanna, G. Madras, Synthesis and structure of nanocrystalline TiO_2 with lower band gap showing high photocatalytic activity, *Langmuir* 20 (2004) 2900–2907.
- [25] R. Gupta, N.K. Eswar, J.M. Modak, G. Madras, Visible light driven efficient N and Cu co-doped ZnO for photoinactivation of *Escherichia coli*, *RSC Adv.* 6 (2016) 85675–85687.
- [26] W. Zhang, M. Wang, W. Zhao, B. Wang, Magnetic composite photocatalyst $\text{ZnFe}_2\text{O}_4/\text{BiVO}_4$: synthesis, characterization, and visible-light photocatalytic activity, *Dalton Trans.* 42 (2013) 15464–15474.
- [27] O. Rosseler, M.V. Shankar, M. Karkmaz-Le Du, L. Schmidlin, N. Keller, V. Keller, Solar light photocatalytic hydrogen production from water over Pt and Au/ TiO_2 (anatase/rutile) photocatalysts: influence of noble metal and porogen promotion, *J. Catal.* 269 (2010) 179–190.
- [28] S.S. Srinivasan, J. Wade, E.K. Stefanakos, Visible light photocatalysis via CdS/TiO_2 nanocomposite materials, *J. Nanomat.* 2006 (2006) 1–7.
- [29] A.P. Jadhav, A. Hussain, J.H. Lee, Y.K. Baek, C.J. Choi, Y.S. Kang, One pot synthesis of hard phase $\text{Nd}_2\text{Fe}_{14}\text{B}$ nanoparticles and $\text{Nd}_2\text{Fe}_{14}\text{B}/\alpha\text{-Fe}$ nanocomposite magnetic materials, *New J. Chem.* 36 (2012) 2405–2411.
- [30] J.K. Cooper, S. Gul, F.M. Toma, L. Chen, Y.-S. Liu, J. Guo, J.W. Ager, J. Yano, I.D. Sharp, Indirect bandgap and optical properties of monoclinic bismuth vanadate, *J. Phys. Chem. C* 119 (2015) 2969–2974.
- [31] P. Kwolek, K. Pilarczyk, T. Tokarski, K. Lewandowska, K. Szacilowski, $\text{Bi}_{1-x}\text{La}_{1-x}\text{VO}_4$ solid solutions: tuning of electronic properties via stoichiometry modifications, *Nanoscale* 6 (2014) 2244–2254.
- [32] M. Xiao, Y. Li, Y. Lu, Z. Ye, Synthesis of ZrO_2 : Fe nanostructures with visible-light driven H_2 evolution activity, *J. Mater. Chem. A* 3 (2015) 2701–2706.
- [33] Y. He, Y. Wang, L. Zhao, X. Wu, Y. Wu, Preparation, characterization and activity evaluation of $\text{V}_{2}\text{O}_5-\text{LaVO}_4$ composites under visible light irradiation, *J. Mol. Catal. A: Chem.* 337 (2011) 61–67.
- [34] J. Fu, S. Cao, J. Yu, Dual Z-scheme charge transfer in $\text{TiO}_2-\text{Ag}-\text{Cu}_2\text{O}$ composite for enhanced photocatalytic hydrogen generation, *J. Materomics* 1 (2015) 124–133.
- [35] H. Huang, D. Li, Q. Lin, W. Zhang, Y. Shao, Y. Chen, M. Sun, X. Fu, Efficient degradation of benzene over $\text{LaVO}_4/\text{TiO}_2$ nanocrystalline heterojunction photocatalyst under visible light irradiation, *Environ. Sci. Technol.* 43 (2009) 4164–4168.
- [36] X. Wu, J. Zhao, S. Guo, L. Wang, W. Shi, H. Huang, Y. Liu, Z. Kang, Carbon dot and BiVO_4 quantum dot composites for overall water splitting via a two-electron pathway, *Nanoscale* 8 (2016) 17314–17321.
- [37] D. Wang, H. Shen, L. Guo, F. Fu, Y. Liang, Design and construction of the sandwich-like Z-scheme multicomponent $\text{CdS}/\text{Ag}/\text{Bi}_2\text{MoO}_6$ heterostructure with enhanced photocatalytic performance in RhB photodegradation, *New J. Chem.* 40 (2016) 8614–8624.
- [38] Z. Chen, F. Bing, Q. Liu, Z. Zhang, X. Fang, Novel Z-scheme visible-light-driven $\text{Ag}_3\text{PO}_4/\text{Ag}/\text{SiC}$ photocatalysts with enhanced photocatalytic activity, *J. Mater. Chem. A* 3 (2015) 4652–4658.
- [39] H.J. Yun, H. Lee, N.D. Kim, D.M. Lee, S. Yu, J. Yi, A combination of two visible-light responsive photocatalysts for achieving the Z-scheme in the solid state, *ACS Nano* 5 (2011) 4084–4090.
- [40] H.G. Kim, E.D. Jeong, P.H. Borse, S. Jeon, K. Yong, J.S. Lee, W. Li, S.H. Oh, Photocatalytic Ohmic layered nanocomposite for efficient utilization of visible light photons, *Appl. Phys. Lett.* 89 (2006) 064103.
- [41] A. Iwase, Y.H. Ng, Y. Ishiguro, A. Kudo, R. Amal, R. G. O. as a solid, state electron mediator in Z-scheme photocatalytic water splitting under visible light, *J. Am. Chem. Soc.* 133 (2011) 11054–11057.
- [42] L. Ding, H. Zhou, S. Lou, J. Ding, D. Zhang, H. Zhu, T. Fan, Butterfly wing architecture assisted $\text{CdS}/\text{Au}/\text{TiO}_2$ Z-scheme type photocatalytic water splitting, *Int. J. Hydrogen Energy* 38 (2013) 8244–8253.
- [43] Z.B. Yu, Y.P. Xie, G. Liu, G.Q.M. Lu, X.L. Ma, H.-M. Cheng, Self-assembled $\text{CdS}/\text{Au}/\text{ZnO}$ heterostructure induced by surface polar charges for efficient photocatalytic hydrogen evolution, *J. Mater. Chem. A* 1 (2013) 2773–2776.
- [44] N. Fu, Z. Jin, Y. Wu, G. Lu, D. Li, Z-scheme photocatalytic system utilizing separate reaction centers by directional movement of electrons, *J. Phys. Chem. C* 115 (2011) 8586–8593.
- [45] X. Wang, G. Liu, L. Wang, Z.G. Chen, G.Q.M. Lu, H.M. Cheng, $\text{ZnO}-\text{CdS}@\text{Cd}$ heterostructure for effective photocatalytic hydrogen generation, *Adv. Energy Mater.* 2 (2012) 42–46.
- [46] Y. Sasaki, H. Nemoto, K. Saito, A. Kudo, Solar water splitting using powdered photocatalysts driven by Z-schematic interparticle electron transfer without an electron mediator, *J. Phys. Chem. C* 113 (2009) 17536–17542.
- [47] S.S.K. Ma, K. Maeda, T. Hisatomi, M. Tabata, A. Kudo, K. Domen, A redox-mediator-Free solar-driven Z-scheme water-splitting system consisting of modified Ta_3N_5 as an oxygen-evolution photocatalyst, *Chem. Eur. J.* 19 (2013) 7480–7486.
- [48] G. QingAlu, Enhanced photocatalytic hydrogen evolution by prolonging the lifetime of carriers in ZnO/CdS heterostructures, *Chem. Commun.* (2009) 3452–3454.
- [49] H. Katsumata, Y. Tachi, T. Suzuki, S. Kaneko, Z-scheme photocatalytic hydrogen production over $\text{WO}_3/\text{g-C}_3\text{N}_4$ composite photocatalysts, *RSC Adv.* 4 (2014) 21405–21409.
- [50] R. Kobayashi, S. Tanigawa, T. Takashima, B. Ohtani, H. Irie, Silver-inserted heterojunction photocatalysts for Z-scheme overall pure-water splitting under visible-light irradiation, *J. Phys. Chem. C* 118 (2014) 22450–22456.
- [51] K. Iwashina, A. Iwase, Y.H. Ng, R. Amal, A. Kudo, Z-schematic water splitting into H_2 and O_2 using metal sulfide as a hydrogen-evolving photocatalyst and reduced graphene oxide as a solid-state electron mediator, *J. Am. Chem. Soc.* 137 (2015) 604–607.
- [52] B.J. Ma, J.S. Kim, C.H. Choi, S.I. Woo, Enhanced hydrogen generation from methanol aqueous solutions over $\text{Pt}/\text{MoO}_3/\text{TiO}_2$ under ultraviolet light, *Int. J. Hydrogen Energy* 38 (2013) 3582–3587.
- [53] F. Shi, L. Chen, M. Chen, D. Jiang, A $\text{g-C}_3\text{N}_4/\text{nanocarbon}/\text{ZnIn}_2\text{S}_4$ nanocomposite: an artificial Z-scheme visible-light photocatalytic system using nanocarbon as the electron mediator, *Chem. Commun.* 51 (2015) 17144–17147.
- [54] R. Ye, H. Fang, Y.-Z. Zheng, N. Li, Y. Wang, X. Tao, Fabrication of $\text{CoTiO}_3/\text{g-C}_3\text{N}_4$ hybrid photocatalysts with enhanced H_2 evolution: z-scheme photocatalytic mechanism insight, *ACS Appl. Mater. Interfaces* 8 (2016) 13879–13889.
- [55] W. Yin, L. Bai, Y. Zhu, S. Zhong, L. Zhao, Z. Li, S. Bai, Embedding metal in the interface of a pn heterojunction with a stack design for superior Z-scheme photocatalytic hydrogen evolution, *ACS Appl. Mater. Interfaces* 8 (2016) 23133–23142.
- [56] L.J. Zhang, S. Li, B.K. Liu, D.J. Wang, T.F. Xie, Highly efficient CdS/WO_3 photocatalysts: z-scheme photocatalytic mechanism for their enhanced photocatalytic H_2 evolution under visible light, *ACS Catal.* 4 (2014) 3724–3729.
- [57] Z. Pan, T. Hisatomi, Q. Wang, S. Chen, M. Nakabayashi, N. Shibata, C. Pan, T. Takata, M. Katayama, T. Minegishi, Photocatalyst sheets composed of particulate $\text{LaMg}_{1/3}\text{Ta}_{2/3}\text{O}_2\text{N}$ and Mo-Doped BiVO_4 for Z-scheme water splitting under visible light, *ACS Catal.* 6 (2016) 7188–7196.
- [58] A. Samal, D.P. Das, K.K. Nanda, B.K. Mishra, J. Das, A. Dash, Reduced graphene

Oxide–Ag₃PO₄ heterostructure: a direct Z-scheme photocatalyst for augmented photoreactivity and stability, *Chem. Asian J.* 11 (2016) 584–595.

[59] W. Zhu, D. Han, L. Niu, T. Wu, H. Guan, Z-scheme Si/MgTiO₃ porous heterostructures: noble metal and sacrificial agent free photocatalytic hydrogen evolution, *Int. J. Hydrogen Energy* 41 (2016) 14713–14720.

[60] C. Feng, S. Wang, B. Geng, Ti (iv) doped WO₃ nanocuboids: fabrication and enhanced visible-light-driven photocatalytic performance, *Nanoscale* 3 (2011) 3695–3699.

[61] M. Sadakane, K. Sasaki, H. Kunioku, B. Ohtani, R. Abe, W. Ueda, Preparation of 3-D ordered macroporous tungsten oxides and nano-crystalline particulate tungsten oxides using a colloidal crystal template method, and their structural characterization and application as photocatalysts under visible light irradiation, *J. Mater. Chem.* 20 (2010) 1811–1818.

[62] X. Yang, F. Qian, Y. Wang, M. Li, J. Lu, Y. Li, M. Bao, Constructing a novel ternary composite (C₁₆H₃₃(CH₃)₃N)₄W₁₀O₃₂/g-C₃N₄/rGO with enhanced visible-light-driven photocatalytic activity for degradation of dyes and phenol, *Appl. Catal. B: Environ.* 200 (2017) 283–296.

[63] J. Xiong, Y. Liu, C. Cao, L. Shen, W. Wu, S. Liang, R. Liang, L. Wu, An architecture of CdS/H₂Ti₅O₁₁ ultrathin nanobelt for photocatalytic hydrogenation of 4-nitroaniline with highly efficient performance, *J. Mater. Chem. A* 3 (2015) 6935–6942.

[64] X. Zhang, Y.L. Chen, R.-S. Liu, D.P. Tsai, Plasmonic photocatalysis, *Rep. Prog. Phys.* 76 (2013) 046401.

[65] P. Zhou, J. Yu, M. Jaroniec, All-solid-state Z-scheme photocatalytic systems, *Adv. Mater.* 26 (2014) 4920–4935.

[66] X. Chen, C. Li, M. Gratzel, R. Kostecki, S.S. Mao, Nanomaterials for renewable energy production and storage, *Chem. Soc. Rev.* 41 (2012) 7909–7937.

[67] M.M. Mohamed, S.A. Ahmed, K.S. Khairou, Unprecedented high photocatalytic activity of nanocrystalline WO₃/NiWO₄ hetero-junction towards dye degradation: effect of template and synthesis conditions, *Appl. Catal. B: Environ.* 150 (2014) 63–73.

[68] K.H. Reddy, S. Martha, K. Parida, Fabrication of novel p-BiOI/n-ZnTiO₃ heterojunction for degradation of rhodamine 6G under visible light irradiation, *Inorg. Chem.* 52 (2013) 6390–6401.